

Central Lancashire Online Knowledge (CLoK)

Title Enhancing the safety of underwater subway tunnels through grouting					
	reinforcement in fault fracture zones				
Type	Article				
URL	https://clok.uclan.ac.uk/id/eprint/55111/				
DOI	https://doi.org/10.1016/j.rineng.2025.104718				
Date	2025				
Citation	Zhang, Hui, Aldahdooh, Majid, Shang, Yong Hui, Yin, Hang, Bashir, Mohammed J.K., Wong, Ai Wei, Olanrewaju, Abdullateef Ashola and Ng, Choon Aun (2025) Enhancing the safety of underwater subway tunnels through grouting reinforcement in fault fracture zones. Results in Engineering, 26. p. 104718.				
Creators	Zhang, Hui, Aldahdooh, Majid, Shang, Yong Hui, Yin, Hang, Bashir, Mohammed J.K., Wong, Ai Wei, Olanrewaju, Abdullateef Ashola and Ng, Choon Aun				

It is advisable to refer to the publisher's version if you intend to cite from the work. https://doi.org/10.1016/j.rineng.2025.104718

For information about Research at UCLan please go to http://www.uclan.ac.uk/research/

All outputs in CLoK are protected by Intellectual Property Rights law, including Copyright law. Copyright, IPR and Moral Rights for the works on this site are retained by the individual authors and/or other copyright owners. Terms and conditions for use of this material are defined in the http://clok.uclan.ac.uk/policies/

ELSEVIER

Contents lists available at ScienceDirect

Results in Engineering

journal homepage: www.sciencedirect.com/journal/results-in-engineering



Research paper

Enhancing the safety of underwater subway tunnels through grouting reinforcement in fault fracture zones

Hui Zhang ^{a,b}, Majed A.A. Aldahdooh ^c, Yong Hui Shang ^b, Hang Yin ^d, Mohammed J.K. Bashir ^e, Ai Wei Wong ^a, Abdullateef Ashola Olanrewaju ^a, Choon Aun Ng ^{a,*}

- ^a Faculty of Engineering and Green Technology, Universiti Tunku Abdul Rahman, 31900 Kampar, Perak, Malaysia
- ^b College of Civil Engineering and Architecture, Huanghuai University, Zhumadian 463000, China
- ^c Department of Facilities and Construction Project Management, International College of Engineering and Management, University of Central Lancashire (UK), P.C. 111, Muscat, Oman
- ^d Institute for Smart City of Chongqing University in Liyang, Liyang 213300, China
- e School of Engineering and Technology, Central Queensland University, 120 Spencer St, Melbourne Vic 3000, Australia

ARTICLE INFO

Keywords: Subsea tunnel Fault fracture zone Grouting reinforcement Control effect Numerical simulation

ABSTRACT

Subsea fault fracture zones pose significant stability challenges and heighten the risk of tunnel face collapse and sudden water inrush during subway construction. Despite the common practice of using grouting reinforcement to stabilize the surrounding rock, there is limited research on its specific control effects. This study addresses this gap by investigating the impact of grouting reinforcement on the safety of subsea tunnels crossing fault fracture zones, using the Qingdao subway project in China as a case study. A coupled numerical model encompassing seepage, stress, and displacement fields was developed via MIDAS/GTS to analyze changes in porewater pressure, seepage velocity, surrounding rock stress, initial support stress, and tunnel displacement before and after grouting. The results demonstrate a significant reduction in porewater pressure and stress concentration postgrouting. The maximum and minimum principal stresses of the initial support were approximately 4.7 MPa and 3.4 MPa, which were found to be within safe limits, indicating a well-designed reinforcement strategy. Additionally, settlement and unlift measurements were 12 mm and 14 mm, representing a 54 % reduction compared to conditions without grouting reinforcement. Both maximum settlement and uplift values were considerably below standard limits of 20 mm, affirming the effectiveness of the grouting measures. The close alignment between field test data and numerical model results validates the model's accuracy. This study provides critical insights and a scientific basis for evaluating and implementing grouting reinforcement in similar subsea tunnel projects, contributing to safer and more efficient construction practices.

1. Introduction

In recent years, due to significant economic and social benefits, urban subway projects have dramatically increased to meet the growing demand for transportation [1]. Currently, subway projects are being developed worldwide, with an operating length of approximately 18, 943.31 km [2,3]. However, modern subway tunnels face more complicated construction environments and operating conditions due to the complex hydrogeological conditions of urban underground space, existing pipelines, and buildings. For instance, the North Extension Line 1 of Shenyang Metro Line 2 crosses under an overpass [4], Phase 1 of Wuhan Metro Line 7 crosses under the Yangtze River [5], and Changsha

Metro Line 3 crosses under the Xiangjiang River [6]. Tunnels that pass beneath rivers, lakes, or seas face significant challenges from ground-water caused by the infiltration of upper water pressure and the change in pore water pressure caused by the excavation of surrounding rock. This can lead to issues such as settlement, landslides, water seepage, and in extreme cases, water inrush—especially in areas with karst, joints, and fracture zones [7,8]. These conditions pose great safety hazards and increases the difficulty of the construction. The grouting reinforcement technology enhances the strength and stability of foundations by injecting grout to fill voids within the soil. This technique exhibits significant potential for application across various fields, including infrastructure construction, geological disaster prevention, and the

E-mail address: ngca@utar.edu.my (C.A. Ng).

^{*} Corresponding author.

restoration of aging buildings. As urbanization accelerates and engineering environments become increasingly complex, the importance of grouting reinforcement technology in improving engineering safety and extending structural lifespan has become more pronounced. Consequently, there is a sustained growth in market demand for this innovative approach.

A notable example is the Jiaozhou Bay subway tunnel in Qingdao, China. The 7800 m tunnel connects Xuejiadao Subdistrict Office in Huangdao District to Tuandao in the main city of Qingdao in the north, crossing underneath the sea at the mouth of Jiaozhou Bay. The tunnel body traverses 18 faults, with relatively broken rock masses. This poses significant technical difficulties and high engineering risks for tunnel construction. Groundwater seepage has a major influence on the stress field and displacement field of tunnel surrounding rock and lining structure, especially under high water pressure. This phenomenon leads to the continuous expansion of the plastic damage zone of surrounding rock, thereby changing the stress state and the deformation of the surrounding rock and lining structure, thus affecting the stability and safety of the tunnel.

Advanced grouting reinforcement measures have been proposed to address these challenges. Grouting reinforcement is influenced by various factors, including grouting materials, pressure, and technique. In engineering practice, the commonly used grouting material is cement slurry, which can form a stable microporous structure in broken rock and soil, and has a significant effect on improving strength. Usually, the grouting pressure is within the range of 4-8 MPa. The use of grouting reinforcement technology is relatively mature and has been applied multiple times in tunnel engineering projects such as Dalian Metro and Changsha Metro. At present, the effectiveness of grouting has been evaluated through theoretical analyses, numerical simulations, and field tests. The traditional theoretical analysis relies on assumptions without considering factors such as material defects and objective boundary conditions. However, field tests require a monitoring or testing space with specific working conditions to be fulfilled. Therefore, it is more feasible to predict the effectiveness of grouting reinforcement by implementing parameter optimization through numerical simulation before tunnel construction. Numerical simulations are mainly based on the theory of elastoplastic mechanics. By solving the elastoplastic mechanical equations (i.e., physical, geometric, and equilibrium equations), the deformation, displacement field, and stress field of tunnel surrounding rock under certain environmental conditions (i.e., dead weight and load) are calculated. The influence of grouting reinforcement on rocks surrounding tunnels crossing fault fracture zones has received minimal investigation, and the effect of fluid-solid coupling on the safety of tunnel excavation has not been considered.

This study addresses the critical gap in understanding the control effects of grouting reinforcement in fault fracture zones in the context of the subway tunnel in Jiaozhou Bay, Qingdao, China. A detailed and scientifically grounded grouting reinforcement scheme was developed based on comprehensive geological survey reports. This study aims to rigorously analyze the effectiveness of grouting reinforcement by establishing coupled seepage field-stress field-displacement field equations and proposing a novel numerical simulation method that considers fluid-solid coupling. The model's feasibility and accuracy were validated using actual field data, ensuring the reliability and stability of the results. This study not only contributes to the current knowledge in the field but also provides a robust scientific basis for the evaluation and implementation of grouting reinforcement measures in similar subsea tunnel projects, significantly contributing to safer and more efficient construction practices.

2. State of the art

Tunnel excavation first removes the rock mass, and then adds support structures. The entire process inevitably disturbs the original geological strata, leading to changes in displacement fields, stress fields,

and seepage fields of the surrounding rock. The degree of these changes is due to the coupling effect of excavation unloading, loading from supporting structures, and variations in porewater pressure [9]. As early as 1969, Peck proposed the calculation formula for settling tanks and noted that the lateral settlement of the surface caused by the excavation of the tunnel entrance follows a normal distribution, providing a basis for tunnel stability analysis [10]. However, these formulas have limited applicability and often fail to account for the changes in water pressure and water-rock coupling effect, and it is even more difficult to reasonably evaluate the reinforcement effect of grouting in locally fractured rock layers. Upon investigation, the experience company considers that the surrounding rock parameters are mostly homogeneous and homogeneous, making it difficult to reasonably define the physical and mechanical parameters of the rock mass after grouting reinforcement of the fractured layer. With the advancement of theoretical research and computer technology, the analysis of complex tunnels using numerical models has become increasingly viable. Pan [11] and Fu [12] established numerical models that simulated the stress and displacement caused by tunnel excavation. Their simulations show that the transverse deformation zone of a tunnel is closely related to the tunnel entrance, with the main disturbance zone being 2-3 times larger than the diameter of the tunnel, and the plastic strain zone of the tunnel surrounding rock mainly locating in the $40^{\circ}-50^{\circ}$ area on both sides of the vault. Moreover, Bernat et al. [13] studied the disturbance laws of the small-curvature-radius tunnel shield construction for the soil mass close to the tunnel, including surface settlement and surrounding rock convergence. Mu et al. [14] examined the damage process and instability failure characteristics of soft rock tunnels, and explored the method of using damage indicators to characterize the failure situation. Di et al. [15] explored the mechanical behaviour of the tunnel supporting structure in fault fracture zones, providing theoretical reference for grouting reinforcement design.

Current research on tunnels in challenging geological conditions often focuses on expansive soils, loess, and rock strata in fracture zones, addressing issues such as the deformation mechanism of tunnel excavation, the reliability of reinforcement measures, and the failure modes of stress concentration zones [16-21]. Compared to ordinary tunnels, the tunnel surrounding rock in fracture zones has weaker overall stability, greater property instability, and higher difficulty in selecting parameters for calculations. Zones with highly developed water systems in the rock strata face additional risks of hydraulic seepage failure. Fault fracture zones with large development scales, soft internal filling medium, and active groundwater are extremely susceptible to instability failure, water inrush, and mud outburst under the action of engineering disturbance, ground stress, and hydraulic pressure. The multistage tectonic movements during fault formation led to strong anisotropy in its internal structure and spatial distribution. This results in highly complex structural development, filling conditions, and hydrogeological conditions. Researchers have extensively studied the mechanisms of water inrush and mud outburst in tunnel fault fracture zones, exploring aspects such as distribution forms, mineral composition, and the relationship between faults and water-bearing bodies. Ishimaru [22] claimed that water inrush is more likely when the fault plane is inclined toward the boundary of the goaf, while Qian et al. [23] identified the mechanism of water inrush in a fault fracture zone. Wang et al. [24] established a three-dimensional model test system to analyze the catastrophic evolution law of water inrush and mud outburst in the tunnel within a fault fracture zone, revealing the response laws of key parameters, such as the displacement around the tunnel, seepage pressure, stress, strain, and protrusion mass, over time in the tunnel in the fault fracture zone without support conditions.

The research work on soil stabilization had been reported by many researchers [25–26]. The current research mainly concentrates on the mechanical mechanism, engineering geological characteristics, groundwater movement law, disaster occurrence mechanism, and advanced investigation of fault fracture zones. However, research on



Fig. 1. The subway tunnel in Jiaozhou Bay.

grouting theory and technology in the face of disasters in fault fracture zones remains insufficient. This limitation is particularly evident from the lack of theoretical support in the design of post-disaster grouting schemes, grouting reinforcement technologies, construction methods and preventive measures, making it difficult to control the construction period, cost, and construction safety. Therefore, effective implementation of grouting reinforcement in geological disaster-affected areas within fault fracture zones has become one of the critical challenges in tunnel construction. Given the deficiency of the existing research and considering the subway engineering background in Qingdao, China, the present study established a seepage field-stress field-displacement field coupling numerical model via MIDAS/GTS software. In addition, the control effect of grouting reinforcement for the underwater tunnel crossing a fault fracture zone was explored by combining the variation laws of porewater pressure, seepage velocity, surrounding rock stress, initial support stress, and displacement before and after grouting reinforcement. This study provides an important and scientific basis for evaluating the reinforcement measures and realizing the refined operation, repair, and maintenance of similar sub-sea tunnels.

3. Methodology

3.1. Project profile

The subway tunnel in Jiaozhou Bay is an important part of Qingdao Metro Line 1 in Qingdao, China. It affects the cut-through speed of Qingdao Metro Line 1 to a certain extent and serves as a node controller. The starting mileage of the line is K23+522, and the ending mileage is K31+723. The total length is about 8.2 km, the sea section is 3.45 km long and the maximum water depth at the tunnel axis in the sea section is 42 m as shown in Fig. 1.

3.2. Hydrogeological conditions and construction conditions

The land section of Xuejiadao area has a groundwater buried depth of 2.1–14 m, with an elevation of 1.58–34.42 m. The movement of groundwater in this region is mainly controlled by the topography, with

the water level fluctuating in response to rainfall by about 1–5 m. In the underwater tunnel area, the groundwater is predominantly rock fissure water, which generally remains in a nonflowing natural state until it is disturbed by the tunnel construction. According to the hydrogeological conditions of the rock strata, structural characteristics such as joints, fissures, and faults not only affect the design load and support structure type of the tunnel, but also affect the stability and construction difficulty of the tunnel. For example, broken rock layers are prone to collapse and water influx, requiring advanced support or grouting reinforcement. The permeability of rock layers affects the flow of groundwater, which in turn affects the construction environment and stability of tunnels, determining the waterproof and drainage design during tunnel construction.

The rock core extracted from the M1Z3-TWG-68 borehole (as shown in Fig. 2) reveals that the rocks within the F4–6 fault fracture zone are highly fractured, with fractures inclined at a steep dip angle of 75°, and diabase veins present at the bottom. The diabase appears to have filled the fault zone during a later geological stage, with the diabase at the bottom remaining relatively intact and exhibiting weak permeability. The width of the primary fracture zone is <5 m Moreover, there is an influence zone on either side of the fracture zone, varying in width from several meters to several dozen meters. This fracture zone is located at tunnel sections K27+180-K27+205, with water permeability of 10–20 (L_u) and a permeability coefficient of (0.15 m/d), indicating a weak permeability level.

According to the advanced forecast results, it was determined that the conditions in the local section of the tunnel are suitable for grouting. Consequently, an advanced pre-grouting construction scheme was implemented specifically for the F4–6 fracture zone. The design parameters for this grouting were developed in compliance with standards such as the "Technical Specification for Construction of Highway Tunnels" (JTG/T 3660–2020) and the "Technical Specification for Cement Grouting Construction of Hydraulic Structures" (SL 62–2014), as detailed in Table 1.

(a)

Project Name: Qingdao Metro Line 1 Engineering survey Section 1 Drilling hole number: M1Z3-TWG-68 Photo Depth: 8.5-12m





Project Name: Qingdao Metro Line 1 Engineering survey Section 1 Drilling hole number: M1Z3-TWG-68 Photo Depth: 12-16.5m



Fig. 2. M1Z3-TWG-68 rock core obtained from a depth of (a) 8.5-12 m, and (b) 12-16.5 m.

Table 1Parameter design for advanced pre-grouting in the local section.

 0 1 0 0	
Range of reinforcement by ejection for water plugging	5 m beyond the contour line
Length of grouting section Diffusion radius of grouting Final grouting pressure Penetration grouting pressure Backfilling grouting pressure Range of grouting rate	30 m 2 m 1.5-3 MPa 0.5-0.7 MPa <0.5 MPa 5-110 L/min
8 8 1 8 1 1 1	

3.3. Numerical analysis of tunnel surrounding rock stability in the fault fracture zone

3.3.1. Seepage field-stress field coupling equation

A microelement is arbitrarily taken to obtain the basic fluid-solid coupling equation based on the assumed soil mass material and seepage. The following assumptions are made in this study:

- 1) The soil mass is completely saturated, homogeneous, and isotropic.
- The physical strength and inertia force of the soil mass are ignored, and the deformation of the soil mass is extremely small.
- Porewater between soil particles is regarded as an incompressible object; and
- 4) The seepage of water in the soil mass follows Darcy's law.

The static equilibrium equation of the soil mass is expressed as follows:

$$\begin{split} & \frac{\partial \sigma_{x}}{\partial x} + \frac{\partial \tau_{yx}}{\partial y} + \frac{\partial \tau_{zx}}{\partial z} = 0, \\ & \frac{\partial \sigma_{y}}{\partial y} + \frac{\partial \tau_{zy}}{\partial z} + \frac{\partial \tau_{xy}}{\partial x} = 0, \\ & \frac{\partial \sigma_{z}}{\partial z} + \frac{\partial \tau_{xz}}{\partial x} + \frac{\partial \tau_{yz}}{\partial y} = 0, \end{split} \tag{1}$$

where σ_x , σ_y , and σ_z represent the normal stresses in the x-, y-, and z-directions, respectively; and τ is the shear stress.

The geometric equation of the soil mass is

$$\varepsilon_{x} = -\frac{\partial u}{\partial x}, \ \gamma_{xy} = -\left(\frac{\partial u}{\partial y} + \frac{\partial v}{\partial x}\right),
\varepsilon_{y} = -\frac{\partial v}{\partial y}, \ \gamma_{yz} = -\left(\frac{\partial v}{\partial z} + \frac{\partial w}{\partial y}\right),
\varepsilon_{z} = -\frac{\partial w}{\partial z}, \ \gamma_{zx} = -\left(\frac{\partial w}{\partial x} + \frac{\partial u}{\partial z}\right),$$
(2)

The physical equations are as follows:

$$\varepsilon_{x} = \frac{1}{E} \left[\dot{\sigma_{x}} - u \left(\dot{\sigma_{y}} + \dot{\sigma_{z}} \right) \right], \quad \gamma_{xy} = \tau_{xy} / G,$$

$$\varepsilon_{y} = \frac{1}{E} \left[\dot{\sigma_{y}} - u \left(\dot{\sigma_{z}} + \dot{\sigma_{x}} \right) \right], \quad \gamma_{yz} = \tau_{yz} / G,$$

$$\varepsilon_{z} = \frac{1}{E} \left[\dot{\sigma_{z}} - u \left(\dot{\sigma_{x}} + \dot{\sigma_{y}} \right) \right], \quad \gamma_{zx} = \tau_{zx} / G,$$
(3)

where E, u, and G represent the elastic modulus, Poisson's ratio, and shear modulus of the soil mass, respectively; σ_x' , σ_y' , and σ_z' represent the effective stresses in different directions. Eq. (4) is acquired through the soil mass's static equilibrium equation (Eq. (1)), geometric equation (Eq. (2)), physical equation (Eq. (3)), and the principle of effective stress proposed by Terzaghi.

$$\begin{split} &d_{1}\frac{\partial^{2}u}{\partial x^{2}}+d_{3}\left(\frac{\partial^{2}u}{\partial y^{2}}+\frac{\partial^{2}u}{\partial z^{2}}\right)+(d_{2}+d_{3})\left(\frac{\partial^{2}v}{\partial x\partial y}+\frac{\partial^{2}w}{\partial x\partial z}\right)-\frac{\partial p}{\partial x}=0\\ &d_{1}\frac{\partial^{2}v}{\partial y^{2}}+d_{3}\left(\frac{\partial^{2}v}{\partial x^{2}}+\frac{\partial^{2}v}{\partial z^{2}}\right)+(d_{2}+d_{3})\left(\frac{\partial^{2}u}{\partial y\partial x}+\frac{\partial^{2}w}{\partial y\partial z}\right)-\frac{\partial p}{\partial y}=0\\ &d_{1}\frac{\partial^{2}w}{\partial z^{2}}+d_{3}\left(\frac{\partial^{2}w}{\partial x^{2}}+\frac{\partial^{2}w}{\partial y^{2}}\right)+(d_{2}+d_{3})\left(\frac{\partial^{2}u}{\partial z\partial x}+\frac{\partial^{2}v}{\partial z\partial y}\right)-\frac{\partial p}{\partial z}=0 \end{split} \tag{4}$$

According to Darcy's law,

$$v_{x} = -\frac{k_{h}}{\gamma_{w}} \frac{\partial p}{\partial x},$$

$$v_{y} = -\frac{k_{h}}{\gamma_{w}} \frac{\partial p}{\partial y},$$

$$v_{z} = -\frac{k_{v}}{\gamma_{w}} \frac{\partial p}{\partial z},$$
(5)

where the unit weight of porewater is $\gamma_w = \rho_w g$.

Eq. (5) is substituted into the differential equation of seepage continuity to obtain Eq. (6):

$$\frac{\partial v_x}{\partial x} + \frac{\partial v_y}{\partial y} + \frac{\partial v_z}{\partial z} = -\frac{\partial}{\partial t} \left(\frac{\partial u}{\partial x} + \frac{\partial v}{\partial y} + \frac{\partial w}{\partial z} \right) \tag{6}$$

Substituting Eq. (5) into Eq. (6) yields:

$$\frac{1}{\gamma_{w}} \left[k_{h} \left(\frac{\partial^{2} p}{\partial x^{2}} + \frac{\partial^{2} p}{\partial y^{2}} \right) + k_{v} \frac{\partial^{2} p}{\partial z^{2}} \right] = \frac{\partial}{\partial t} \left(\frac{\partial u}{\partial x} + \frac{\partial v}{\partial y} + \frac{\partial w}{\partial z} \right)$$
(7)

Finally, the seepage–stress coupling equation set can be obtained by using Eqs. (4) and (7) simultaneously, as shown as follows:

$$G\nabla^{2}u - (\lambda + G)\frac{\partial\varepsilon_{v}}{\partial x} - \frac{\partial p}{\partial x} = 0,$$

$$G\nabla^{2}v - (\lambda + G)\frac{\partial\varepsilon_{v}}{\partial y} - \frac{\partial p}{\partial y} = 0,$$

$$G\nabla^{2}w - (\lambda + G)\frac{\partial\varepsilon_{v}}{\partial z} - \frac{\partial p}{\partial z} = 0,$$

$$H|\Gamma_{1} = \varphi_{1}(x, y, z, t),$$

$$\frac{1}{r_{w}} \left[k_{h} \left(\frac{\partial^{2}p}{\partial x^{2}} + \frac{\partial^{2}p}{\partial y^{2}} \right) + k_{v}\frac{\partial^{2}p}{\partial z^{2}} \right] = \frac{\partial\varepsilon_{v}}{\partial t}$$
(8)

where,
$$\nabla^2 = \frac{\partial^2}{\partial x^2} + \frac{\partial^2}{\partial y^2} + \frac{\partial^2}{\partial z^2}$$
; $\varepsilon_v = \varepsilon_x + \varepsilon_y + \varepsilon_z = -\left(\frac{\partial u}{\partial x} + \frac{\partial v}{\partial y} + \frac{\partial w}{\partial z}\right)$ and λ and G are the Lame's constant and shear modulus, respectively.

3.3.2. Basic equations of finite element method (FEM)

The FEM-based fluid–solid coupling model is calculated by Galerkin method, as shown below:

$$\int ([B]^{T}[C][B]) dV\{H\} + \int_{V} (\lambda[N]^{T}[N][N]) dV\{H\}t = q \int_{S} ([N]^{T}) dS$$
 (9)

where [B] is the momentum grade matrix; [C] is the permeability coefficient matrix of the element; $\{H\}$ denotes the node waterhead vector; [N] represents the shape function vector; t denotes time; S is the unit area of the element; $\{H\}t = \frac{\partial h}{\partial t}$ is the time-varying waterhead; $\lambda = m_w \gamma_w$; and q is the edge quality of the element. Eq. (9) is simplified as follows:

$$[K]{H} + [M]{H}t = [Q]$$
(10)

3.4. Constitutive model

The elastoplastic material models in MIDAS/GTS include Mohr–Coulomb, von Mises, and Hoek–Brown models. In this study, the Mohr–Coulomb model was mainly adopted, and the yield function is expressed by Eq. (11).

The range of the Lode angle in the above formula is $0^{\circ} \le \theta \le 60^{\circ}$. When the Lode angle falls into the range of $-30^{\circ} \le \theta \le 30^{\circ}$, the above formula will be expressed differently.

3.4.1. Eigenvalue of elastoplastic materials

Table 2 shows the data types of input into the elastoplastic model.

3.4.2. Strain-softening model

The strain–softening constitutive relation of MIDAS/GTS is shown in Fig. 3. The stress–strain relation curve consists of three parts, namely, the linear part reaching the maximum shear strength, the softening part from the maximum shear strength to the residual strength, and the part maintaining the residual strength.

The yield function of the strain–softening model is expressed as follows:

$$F\left(\underline{\sigma}, \varepsilon_p\right) = \sqrt{3J_2} - \sqrt{3c_u},\tag{12}$$

where $J_2 = \frac{1}{6} \left[\left(\sigma_x - \sigma_y \right)^2 + \left(\sigma_y - \sigma_z \right)^2 + \left(\sigma_z - \sigma_x \right)^2 \right] + \tau_{xy}^2 + \tau_{yz}^2 + \tau_{zx}^2$ represents the second invariant of the stress deviator.

The shear strength varies with the value of the total equivalent plastic strain.

$$C_{x} = \begin{cases} C_{x} & \text{when } \varepsilon_{F} = 0\\ C_{x} - R\varepsilon_{p} & \text{when } 0 < \varepsilon_{F} \leq \varepsilon_{pr},\\ C_{r} & \text{when } \varepsilon_{p} > \varepsilon_{F} \end{cases}$$

$$(13)$$

where C_u is the maximum strength (kN/m²); C_r is the residual viscous shear strength (kN/m²); ε_p is the total equivalent plastic strain, which is dimensionless; ε_{pr} is the plastic strain at the residual strength line–softening line crossing position, which is dimensionless; and R is the softening rate (kN/m²).

3.5. Numerical analysis: calculation models and key parameters

The fault fracture zone F4–6 of the subway tunnel in Jiaozhou Bay was modeled and analyzed. The cross-section of the tunnel in this range is designed as a four-centered circle, with a diameter of 12.4 m and height of 8.76 m. The tunnel excavation process is simulated without considering the influence of other constructions on the mechanical behavior of the main tunnel construction, focusing solely on one main tunnel as the simulation object. The origin of the model is taken at the starting point of the tunnel, with the longitudinal direction of the tunnel as the Y-axis, the direction in the horizontal plane as the X-axis, and the vertical direction as the Z-axis. The calculation model is shown in Fig. 4,

$$f(I_1, J_2, \theta_0) = -\frac{1}{3} I_1 \sin \phi + \sqrt{J_2} \sin \left(\theta_0 + \frac{\pi}{3}\right) - \frac{1}{\sqrt{3}} \sqrt{J_2} \cos \left(\theta_0 + \frac{\pi}{3}\right) \sin \phi - \cos \phi$$

$$= -I_1 \sin \phi + \left[\frac{3(1 + \sin \phi)\sin \theta_0 + \sqrt{3}(3 - \sin \phi)\cos \theta_0}{2}\right] \sqrt{J_2} - 3\cos \phi$$

$$= 0$$

$$(11)$$

where $I_1 = \sigma_x + \sigma_y + \sigma_z$ is the first invariant of the stress tensor; $J_2 = \frac{1}{6} \left[\left(\sigma_x - \sigma_y \right)^2 + \left(\sigma_y - \sigma_z \right)^2 + \left(\sigma_z - \sigma_x \right)^2 \right] + \tau_{xy}^2 + \tau_{yz}^2 + \tau_{zx}^2$ is the second invariant of the stress deviator; $J_3 = s_x s_y s_z + 2 \tau_{xy} \tau_{yz} \tau_{zx} - s_x \tau_{yz}^2 - s_y \tau_{zx}^2$

 $s_z \tau_{xy}^2$ is the third invariant of the stress deviator; $\theta = \frac{1}{3} \cos^{-1} \left(\frac{3\sqrt{3}}{2} \frac{J_3}{\frac{3}{2}} \right)$ is

the Lode angle (°); (s_x, s_y, s_z) is the stress deviator; σ_c and σ_r are the uniaxial compressive strength (MPa).

and the dimension in direction $X \times Y \times Z$ is 120 $m \times 40 m \times 110 m$.

According to the geological survey data, the soil mass in the model can be divided into three types: weakly weathered layer, slightly weathered layer, and fault fracture zone. The first layer is the weakly weathered layer of about 14 m in thickness. The second layer consists of a slightly weathered layer of about 96 m in thickness, and, lastly, the fault fracture zone. In Fig. 4, the different geological layers are visually represented. The light-yellow part indicates the slightly weathered layer, and the yellowish-brown part is the fault fracture zone, both of which are 20 m in width. The weakly weathered layer, slightly

Table 2 Elastoplastic eigenvalue.

Eigenvalue	
E	
μ	
C	
φ	
von Mises and Tresca	
Mohr-Coulomb	

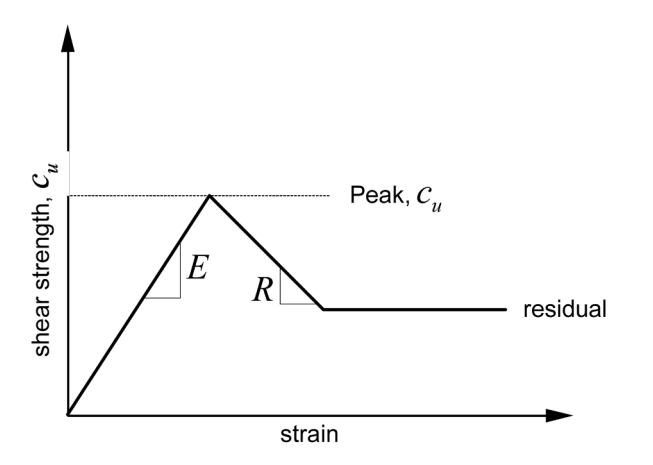


Fig. 3. Strain-softening constitutive relation.

weathered layer, and fault fracture zone are simulated by 3D solid elements that conform to the strain–softening yield criterion. The grouting reinforcement circle is simulated using 3D solid elements following the Mohr–Coulomb elastoplastic yield criterion. The initial support is simulated using 2D plate elements that comply with the elastic yield criterion. The model uses unit sets for hierarchical assignment based on actual geological survey data.

3.6. Model parameter selection and boundary conditions

When the tunnel passes through the fault fracture zone, reinforcement measures, such as advanced small pipes and hollow self-drilling pipe shed, are usually adopted that create a reinforcement zone around the tunnel. In the simulation, the reinforcement measures are represented by improving the parameters of the soil mass near the tunnel excavation. The reinforcing effect of the steel arch and steel mesh are also incorporated by similarly adjusting the parameters. The influence of the steel arch and steel mesh is simulated by converting the

elastic modulus of steel arch into an equivalent modulus for shotcrete, and the calculation formula is shown as follows [24]. The boundary condition is fixed around the tunnel ring.

$$E = E_0 + \frac{S_g \times E_g}{S_c},\tag{14}$$

where E is the elastic modulus of concrete after conversion, MPa; E_0 is the original elastic modulus of concrete, MPa; S_g is the sectional area of the steel arch, m²; E_g is the elastic modulus of steel, MPa; and S_c is the sectional area of concrete, m².

The parameters are selected in accordance with the Detailed Geotechnical Engineering Survey Report of Bid Section 1 of Qingdao Metro Line 1 and Technical Manual for Railway Engineering Design-Tunnel. The physical and mechanical parameters of the surrounding rock and initial support after considering the influence of the steel mesh and steel arch on shotcrete are listed in Table 3.

3.7. Simulation of tunnel construction conditions

In this study, the tunnel excavation process is simulated via finite element software MIDAS/GTS to analyze the changes in the seepage field and surrounding rock stress and strain after tunnel excavation. Before excavation, the initial seepage field of the surrounding rock is first analyzed. The excavation process is simulated in two major parts. First, the seepage field change during excavation is analyzed in the excavation simulation. Subsequently, the initial support structures are applied in excavated tunnel face in the simulation.

The basic analysis steps of the stress field are as follows. First, the initial stress field of the surrounding rock is analyzed before excavation. Second, the distribution of surrounding rock stress and strain and their changes induced by excavation are analyzed. Finally, similar to the seepage field analysis, after each excavation step, initial supports are applied to the tunnel face. The analysis of the stress and seepage fields is repeated from Step 1 to Step 2, with the proceeding of tunnel excavation until the last initial support is installed.

In this study, the stability of surrounding rock in the tunnel crossing the fault fracture zone is mainly investigated. During simulation, the tunnel excavation steps are reasonably simplified, and the full-section tunnel excavation method is adopted. When the slightly weathered layer is excavated, the excavation footage is 2 m, and every ring is supported upon excavation. When the excavation proceeds to the fault fracture zone, the excavation footage is changed to 0.5 m, and the stability of tunnel surrounding rock in case of excavation by 25 m is analyzed.

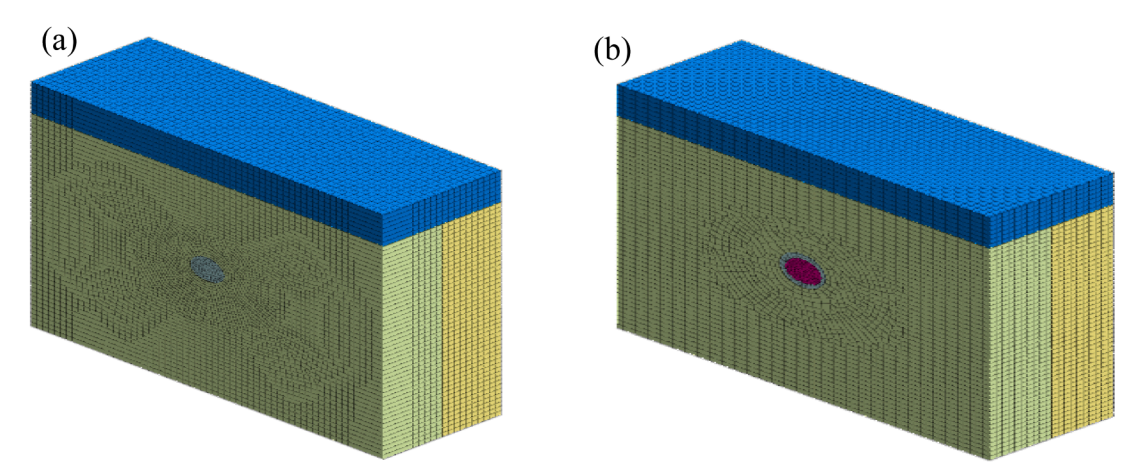


Fig. 4. Numerical calculation model (a) without grouting reinforcement, and (b) with grouting reinforcement.

Table 3Physical and mechanical parameter values of surrounding rock and supporting structure.

Lithology	Volume weight $(\gamma/k\mathbf{N}\cdot\mathbf{m} - 3)$	Elastic modulus (<i>E/GPa</i>)	Poisson's ratio (µ)	Maximum cohesion (C/MPa)	Internal friction angle $(arphi/^{\circ})$	Permeability coefficient (m/day)
Weakly weathered layer	20	7.2	0.312	0.72	24	0.03
Slightly weathered layer	22	10.1	0.28	1.05	24	0.04
Fault fracture zone	21	8.1	0.28	0.8	24	0.15
Grouting reinforcement zone	22	12	0.3	1.2	30	0.01
30-cm C25 shotcrete	22	27	0.2	_	_	_
φ25 hollow bolt	_	450	0.3	-	-	_

4. Result and discussions

4.1. Stability analysis of tunnel construction in the fault fracture zone without grouting reinforcement

4.1.1. Porewater pressure field analysis

The porewater pressure changes of surrounding rock during tunnel excavation are illustrated in Fig. 5. Without reinforcement, the porewater pressure of the surrounding rock is layered before excavation, but it undergoes significant changes after excavation. This results in the formation of a funnel-shaped porewater pressure zone around the excavated face, and a decrease in porewater pressure around the tunnel. Simultaneously, the porewater pressure of the surrounding rock and tunnel face gradually decreases as excavation proceeds. When the tunnel face reaches the fault fracture zone, the porewater pressure values change greatly, which considerably affects the stability of the surrounding rock. Therefore, monitoring of the deformation of surrounding rock and the initial support at this position during construction must be strengthened.

4.1.2. Stress analysis of surrounding rock

Fig. 6 shows the cloud maps of the maximum and minimum principal stresses of the surrounding rock during tunnel excavation. It is observed that due to stress release after tunnel excavation, stress is redistributed, and the maximum principal stress is symmetrically distributed along the tunnel axis, and it changes significantly as excavation approaches the fault fracture zone, reaching a maximum value of approximately 0.4 MPa. As excavation continues, the maximum principal stress decreases slowly; Meanwhile, the minimum principal stress of the surrounding rock changes greatly after tunnel excavation, also presenting a symmetrical distribution along the tunnel axis. As the tunnel face advances, the minimum principal stress gradually increases to about -5.5 MPa. The profile maps of surrounding rock stress indicate that the peak value of the maximum principal stress appears at the tunnel bottom and vault, while the peak value of the minimum principal stress appears at the left and right arch waists. Therefore, these positions require close attention during tunnel construction to ensure the overall stability of the tunnel.

In short, during tunnel excavation, the maximum and minimum principal stresses of the surrounding rock change significantly. As the excavation proceeds toward the fault fracture zone, these stresses experience notable alterations before gradually stabilizing as the

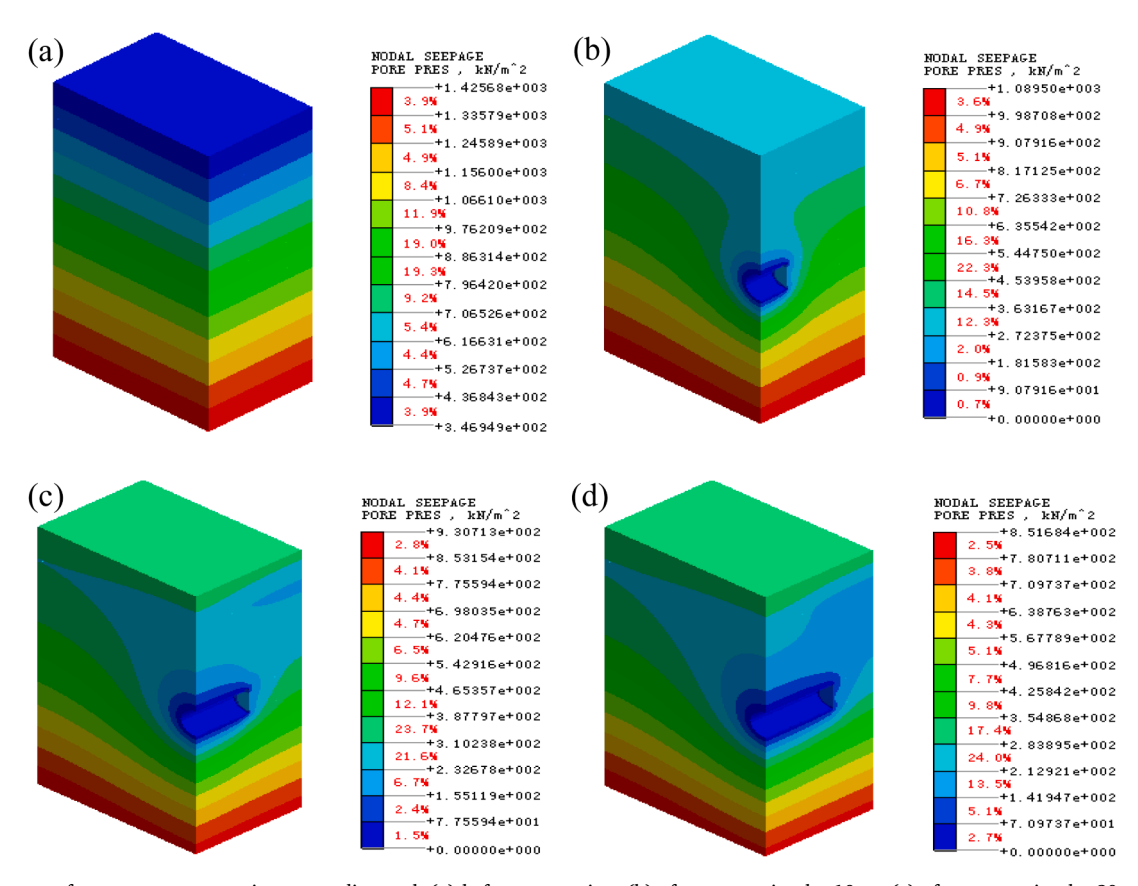


Fig. 5. Cloud maps of porewater pressure in surrounding rock (a) before excavation, (b) after excavation by 10 m, (c) after excavation by 20 m, and (d) after excavation by 25 m.

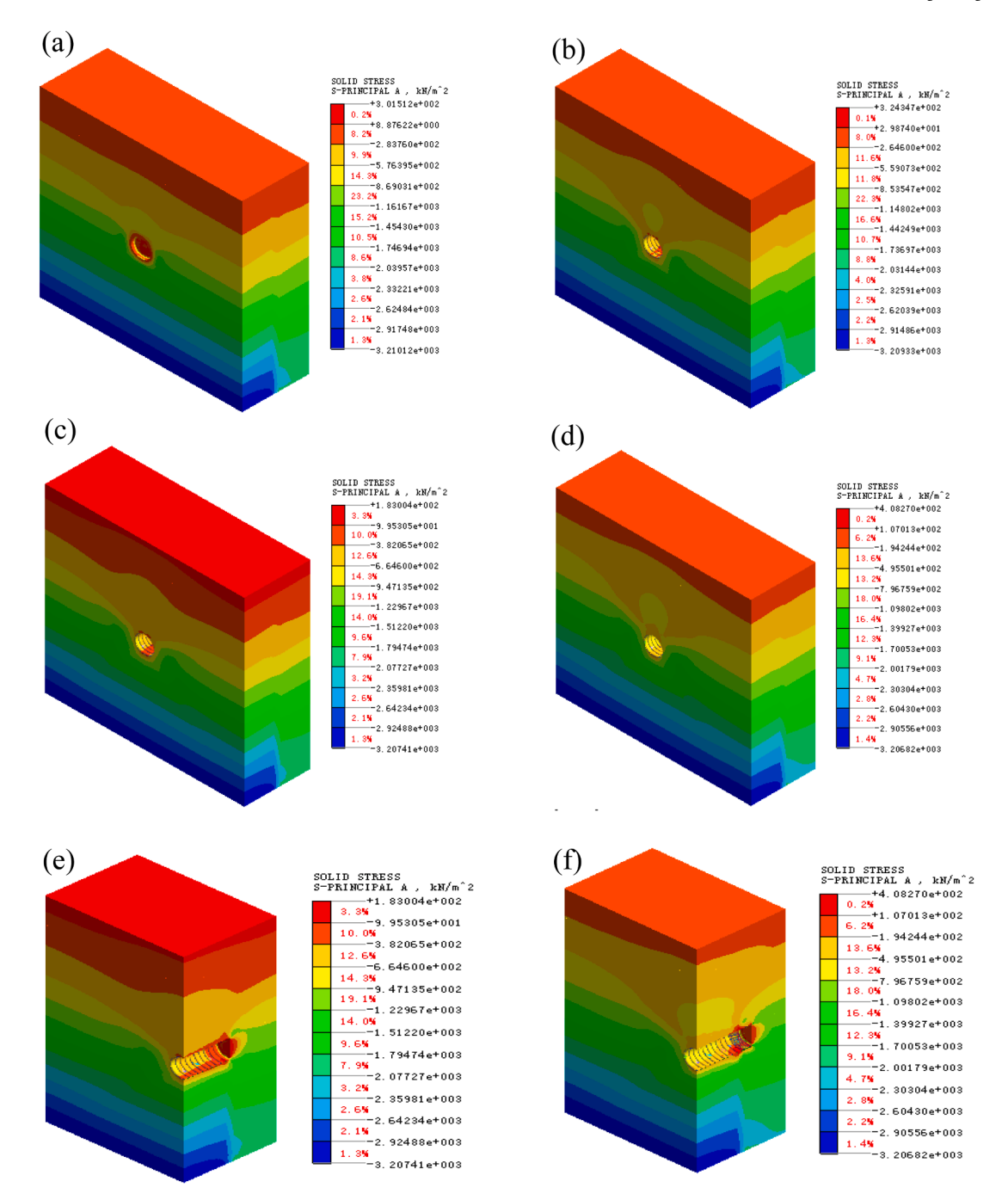


Fig. 6. Cloud maps of maximum principal stress in surrounding rock after excavation by (a) 2 m, (b) 10 m, (c) 20 m, (d) 25 m, (e) 20 m (cross-sectional view), and (f) 25 m (cross-sectional view).

excavation continues.

4.1.3. Stress analysis of initial support

The cloud maps of the maximum and minimum principal stresses of the initial support during tunnel excavation are displayed in Figs. 7 and 8, respectively. Based on Fig. 7, the maximum principal stress in the initial support changes significantly during construction. This stress increases substantially as the tunnel face approaches the fault fracture zone. The maximum principal stress reaches about 2.1 MPa after the initial support is completed by 10 m and about 11 MPa by 25 m, which is 4.6 times of the original value. Throughout the whole excavation process, the maximum principal stress is always considerably greater than the design tensile strength of the initial support concrete, failing to meet

the safety requirements for the initial support specified in the relevant code. Thus, the safety and stability of the surrounding rock during excavation are compromised, posing potential safety hazards.

Fig. 8 shows that the minimum principal stress in the initial support gradually increases after tunnel excavation. It rises from about $-10\,\mathrm{MPa}$ after $10\,\mathrm{m}$ of support completion to approximately $-13\,\mathrm{MPa}$ by $25\,\mathrm{m}$, increasing to $1.3\,\mathrm{times}$ the original value. The profile map in each stage of the initial support indicates that after the construction of the initial support, the minimum principal stress always appears at left and right walls, while the maximum principal stress always appears at the inverted arch. Hence, these two positions should receive special attention during tunnel construction, and the monitoring measurement frequency should be increased to ensure that the settlement value in the

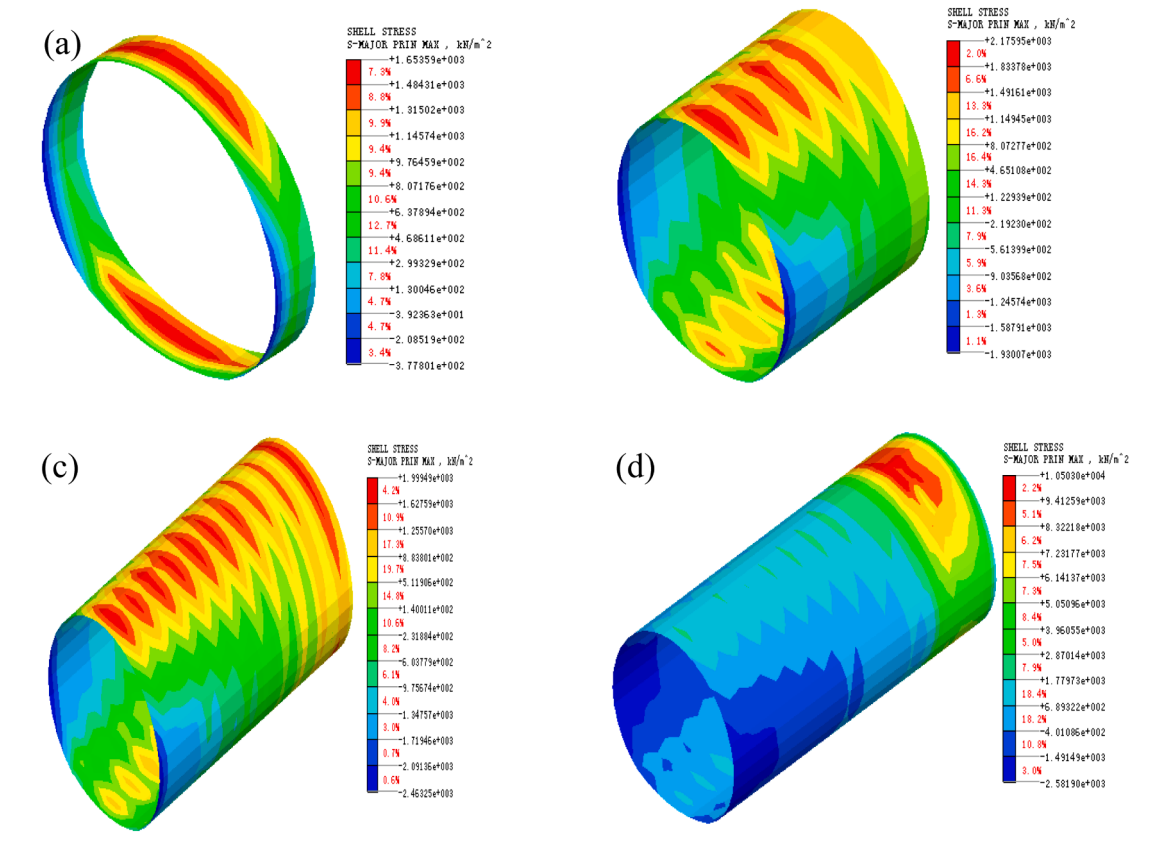


Fig. 7. Cloud maps of maximum principal stress of initial support by (a) 2 m, (b) 10 m, (c) 20 m, and (d) 25 m.

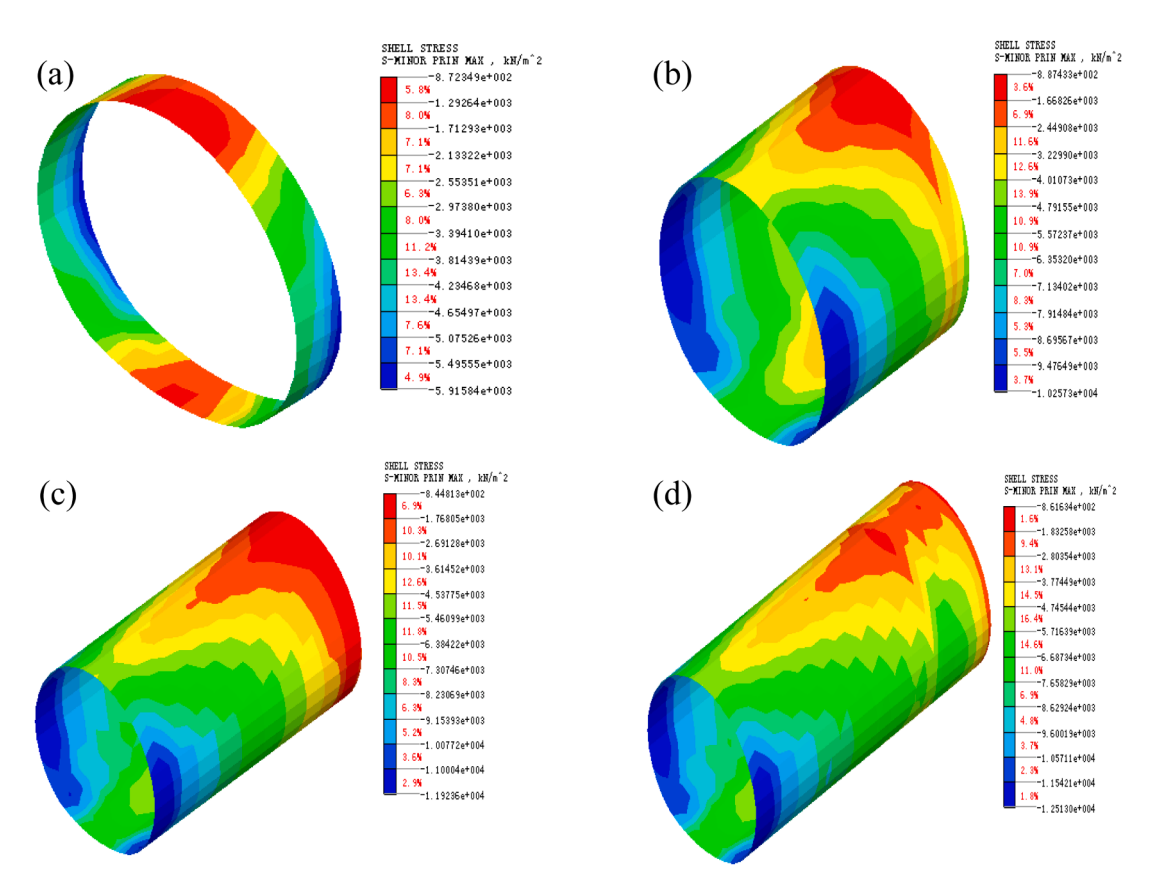


Fig. 8. Cloud maps of minimum principal stress of initial support by (a) 2~m, (b) 10~m, (c) 20~m, and (d) 25~m.

process of tunnel construction conforms to the relevant code and design requirements.

To sum up, as the tunnel excavation progresses, the maximum and minimum principal stress values of the initial support gradually increase. When the tunnel face reaches the fault fracture zone, the maximum principal stress of the initial support is considerably greater than the design tensile strength of the initial support concrete. In such cases, the safety of the initial support cannot be guaranteed, and the stability of the surrounding rock fails to meet the design requirements, resulting in hidden dangers.

4.1.4. Displacement analysis

The displacement cloud maps of the surrounding rock in the Z-direction during tunnel excavation are as shown in Fig. 9. These maps indicate that during excavation, the displacement at the excavated face increases rapidly. However, as the excavation proceeds, the surrounding rock and initial support undergo coordinated deformation, which eventually stabilizes. After the tunnel excavation is complete, the maximum displacement in the Z-direction is observed at the top and bottom of the tunnel, with the maximum settlement at the vault reaching 26 mm and the maximum uplift at the inverted arch reaching 31 mm.

The analysis shows that the displacement of the tunnel wall progressively increases during construction. Particularly, as excavation advances toward fault fracture zones, there is a significant surge in displacement. However, beyond this stage, the displacement at various positions along the tunnel wall does not continue to increase proportionally with ongoing tunneling.

4.2. Construction stability analysis of the fault fracture zone in the subway tunnel of Jiaozhou Bay under grouting reinforcement conditions

4.2.1. Analysis of porewater pressure field

Fig. 10 shows the changes in porewater pressure of surrounding rock during excavation. Prior to excavation, the distribution of porewater pressure in the surrounding rock is relatively uniform. After tunnel excavation, the porewater pressure of surrounding rock decreases significantly as compared to the initial porewater pressure, indicating great seepage force within this range. On the contrary, the porewater pressure beyond this range shows minimal changes from the initial conditions, with negligible seepage forces that can be disregarded. Before the tunnel excavation to the fault fracture zone, the porewater pressure of the surrounding rock and tunnel face does not change considerably. Nevertheless, upon advancing to the fault fracture zone, the porewater pressure at the tunnel face drops sharply and then decreases slowly.

To sum up, after grouting reinforcement, the porewater pressure field of the surrounding rock does not undergo great changes post-excavation, but it is redistributed within a specific area around the tunnel. Conversely, the porewater pressure field beyond the range remains largely unchanged compared to the initial state. As the excavation advances to the fault fracture zone, noticeable changes in porewater pressure of the surrounding rock occur. Compared to the situation without grouting reinforcement, the porewater pressure is obviously reduced after grouting reinforcement, which exerts a positive effect on improving the stability of the tunnel face and surrounding rock.

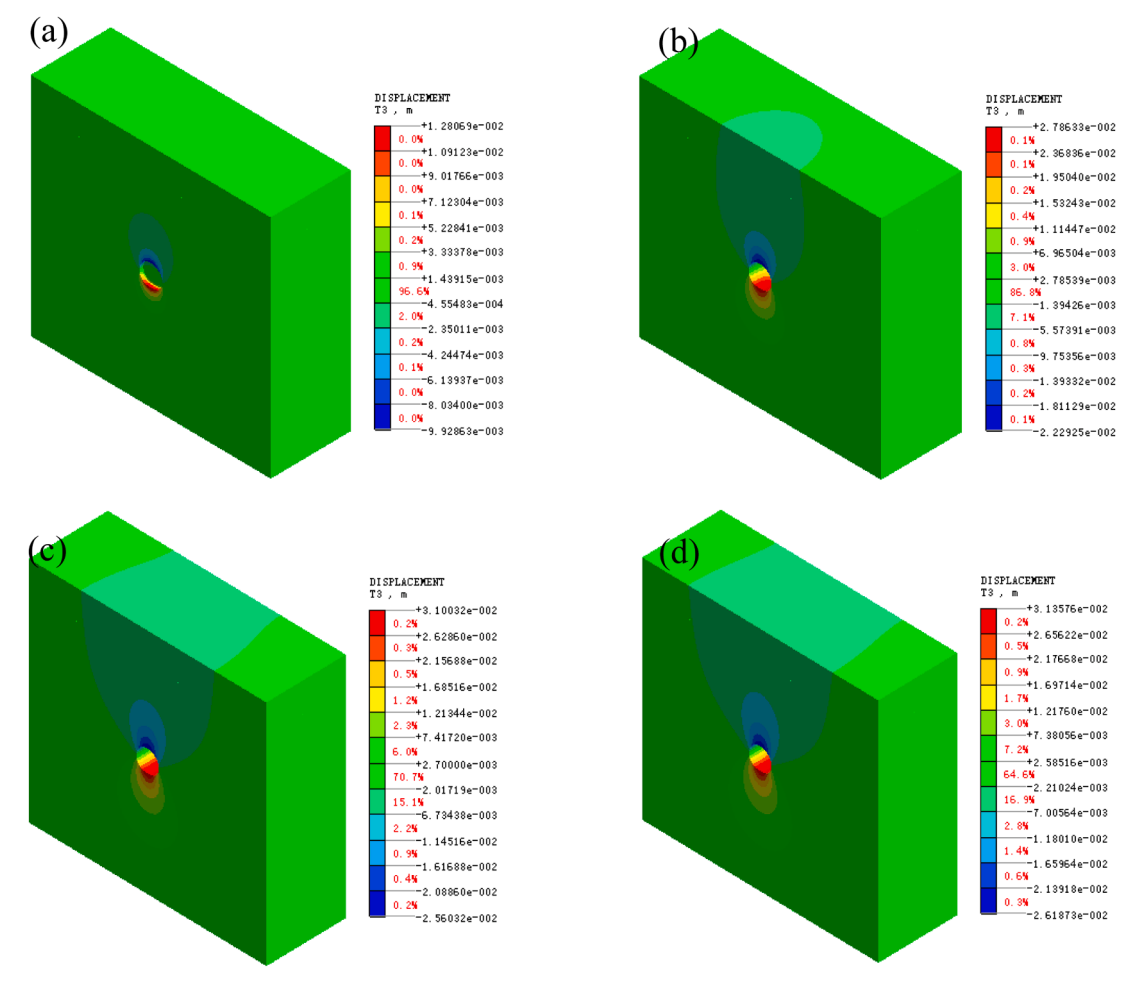


Fig. 9. Displacement cloud maps in the Z-direction after excavation by (a) 2 m, (b) 10 m, (c) 20 m, and (d) 25 m.

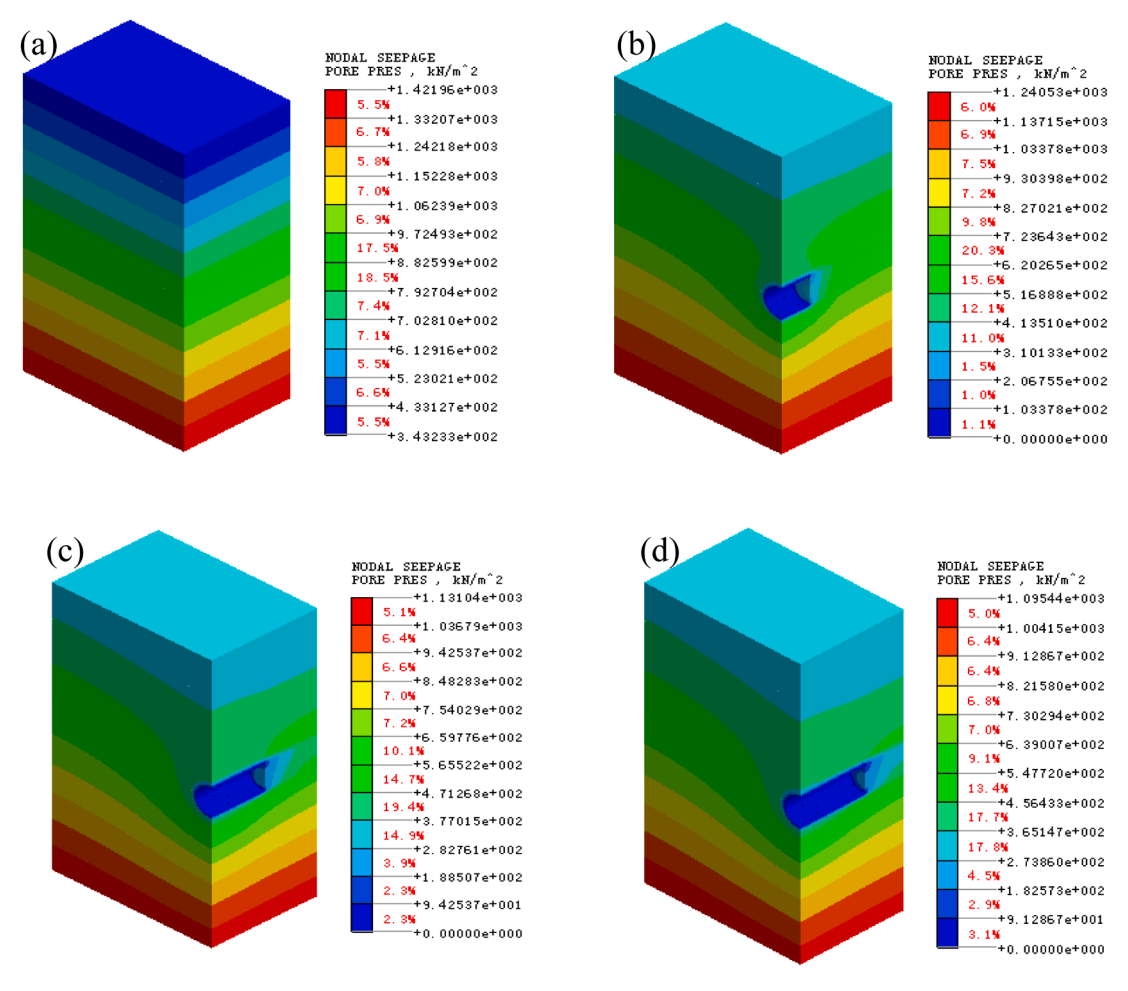


Fig. 10. Porewater pressure cloud maps of surrounding rock (a) before excavation, (b) after excavation by 10 m, (c) after excavation by 20 m, and (d) after excavation by 25 m.

4.2.2. Stress field analysis of surrounding rock

The cloud maps of the maximum and minimum principal stresses of the surrounding rock during excavation are exhibited in Figs. 11 and 12, respectively. After grouting reinforcement, the maximum principal stress and tensile stress within the tunnel cavern are reduced, alongside a decrease in the low-stress zone. The maximum principal stress value of the surrounding rock around the tunnel also decreases. Similarly, the minimum principal stress zone of the tunnel surrounding rock reduces after grouting, as well as the minimum principal stress values. The

profile maps of the surrounding rock stress indicate that the maximum principal stress still appears at the vault and tunnel bottom after grouting reinforcement while the minimum principal stress is located at the left and right arch waists.

In summary, grouting reinforcement effectively reduces the maximum and minimum principal stress zones of the surrounding rock around the tunnel, allowing the surrounding rock to utilize its natural bearing capacity. In addition, grouting can favorably improve the mechanical properties of the surrounding rock in the tunnel and reduce the

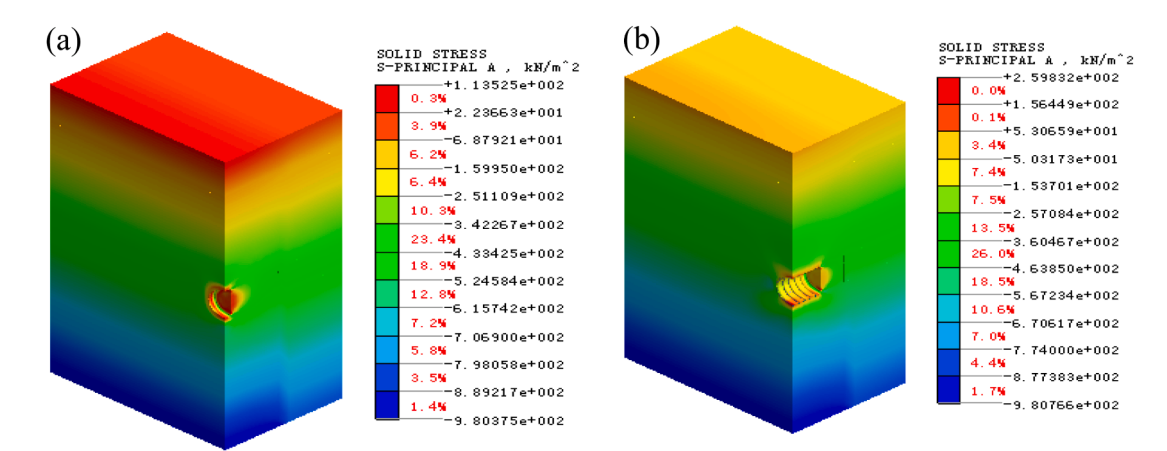


Fig. 11. Cloud maps of maximum principal stress of surrounding rock after excavation by (a) 2 m, and (b) 10 m.

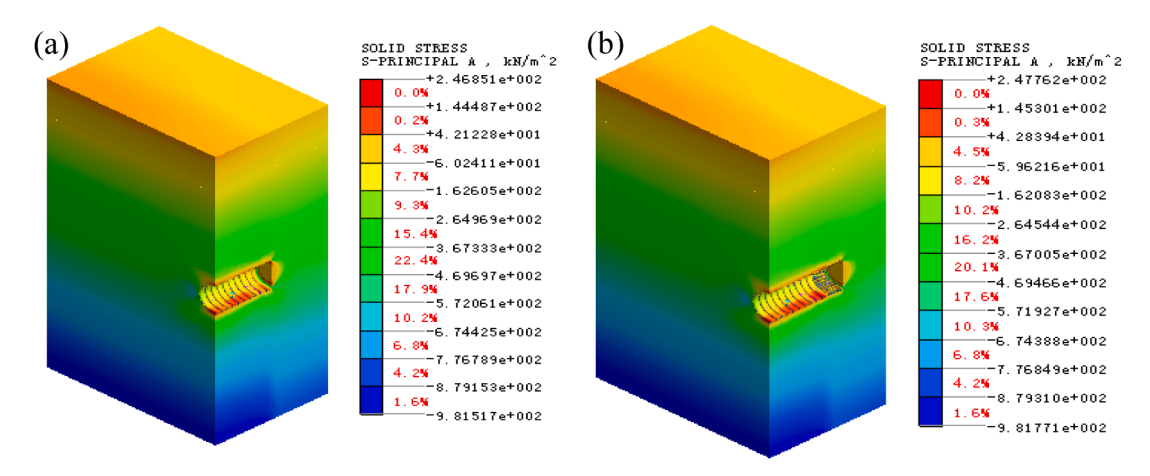


Fig. 12. Cloud maps of minimum principal stress of surrounding rock after excavation by (a) 20 m, and (b) 25 m.

external load on the tunnel structure.

4.2.3. Stress analysis of initial support

Figs. 13 and 14 are the cloud maps of the maximum and minimum principal stress of the initial support during tunnel excavation. The maximum principal stress value of the initial support varies as the tunnel excavation progresses, but as shown in Fig. 13, the changes are not particularly large. After the initial support of the tunnel is completed by 10 m, the maximum principal stress is about 2.1 MPa. Once the initial support is extended to 25 m, the maximum principal stress increases to approximately 4.7 MPa, giving a rise of 2.6 MPa. During excavation, the maximum stress value of the initial support remains lower than the initial support stress without grouting reinforcement, thereby ensuring the stability of the surrounding rock during tunnel excavation. As tunneling proceeds, the minimum principal stress gradually increases. After the initial support is completed by 10 m, the minimum principal stress is about -2.9 MPa. When the initial support is completed by 25 m, the value is approximately -3.4 MPa. The minimum principal stress value of the initial support remains negative during tunnel excavation, and it is consistently lower than the design compressive strength of concrete.

From the profile map of the minimum principal stress cloud map of the initial support (Fig. 14), it is seen that after the construction of the initial support, the minimum principal stress consistently appears at the left and right side walls, while the maximum principal stress occurs at the inverted arch. These two positions should be closely monitored during construction, and frequent measurement should be done to ensure that the settlement value during tunnel construction conforms to the relevant standard and design requirements.

Overall, the maximum and minimum principal stresses caused by the initial support gradually increase as the excavation progresses. Upon advancement to the fault fracture zone, the maximum principal stress of the initial support is about 4.7 MPa, while the minimum principal stress is about 3.4 MPa, both of which are smaller than the design strength of concrete. Compared to the situation before grouting reinforcement, the stress value of the initial support after grouting reinforcement constantly meets the design and code requirements, and the stability of the surrounding rock satisfies the relevant requirements.

4.2.4. Displacement analysis

The displacement cloud maps of the surrounding rock in the Z-direction during tunnel excavation are displayed in Fig. 15. After grouting reinforcement, the maximum settlement in the Z-direction of the surrounding rock is 12 mm, and the maximum uplift is 14 mm. These values represent a reduction of approximately 14 mm (54 %) in settlement and 17 mm (54 %) in uplift compared to the conditions without grouting reinforcement. Besides, the areas with relatively large settlement and uplift of the surrounding rock in the Z-direction are reduced to some extent after grouting.

This indicates that the displacement of the surrounding rock is effectively controlled after grouting reinforcement. Upon excavation to the fault fracture zone, the maximum settlement of the tunnel vault is 12 mm, and the maximum uplift is 14 mm, neither of which exceeds the allowable displacement limit of 20 mm, demonstrating that the stability of the surrounding rock meets design and code requirements after grouting reinforcement.

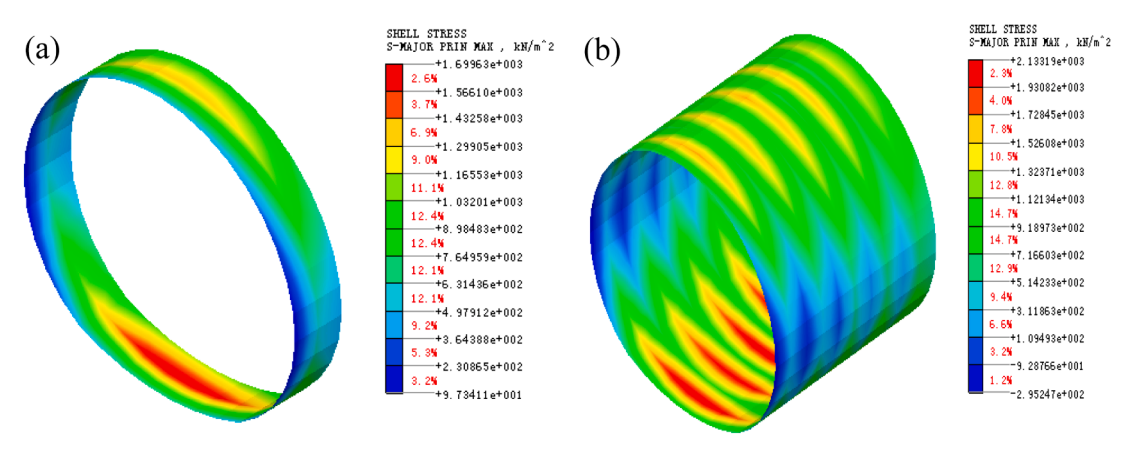


Fig. 13. Maximum principal stress cloud maps of initial support by (a) 2 m, and (b) 10 m.

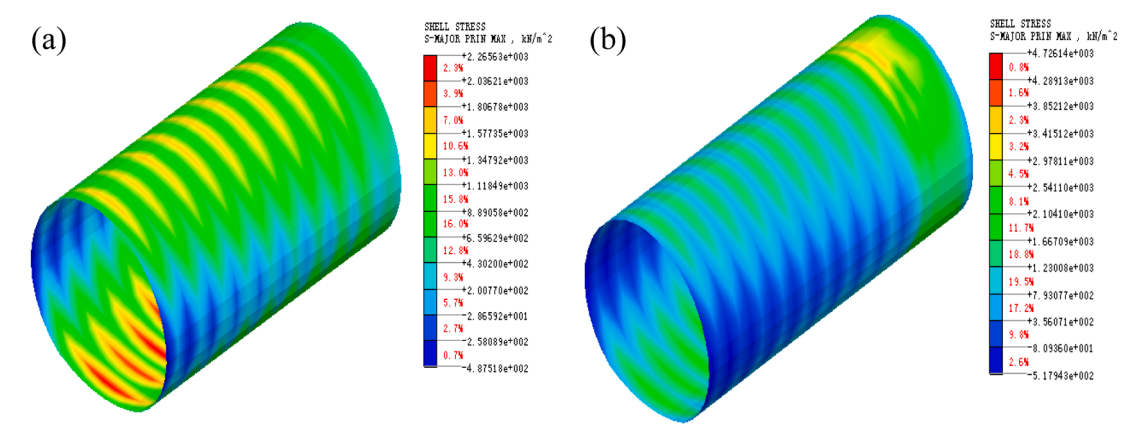


Fig. 14. Minimum principal stress cloud maps of initial support by (a) 20 m, and (b) 25 m.

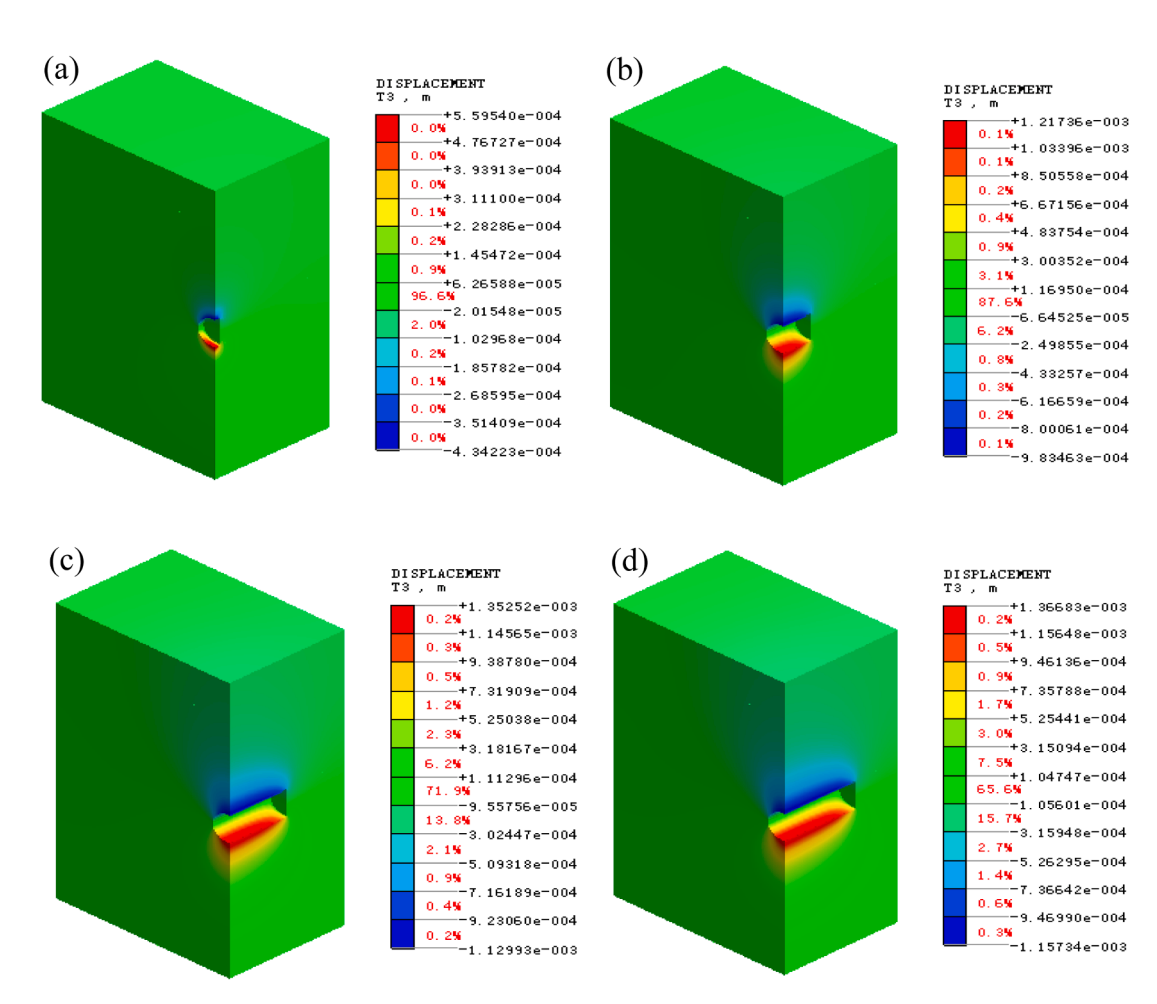


Fig. 15. Displacement cloud maps in the Z-direction after excavation by (a) 2 m, (b) 10 m, (c) 20 m, and (d) 25 m.

4.3. Comparative analysis of field monitoring data and simulation results

Considering the topography, landforms, and the special geological conditions of tunnel engineering, data of the K27+180 section, located in the F4–6 fault fracture zone, are collected during the excavation of the subway tunnel in Jiaozhou Bay. In this section, in this section, monitoring data primarily focuses on vault settlement and clearance convergence. The collected data are then sorted to summarize and analyze the deformation patterns of the surrounding rock and the support structures during tunnel excavation. Through this analysis, the stability of the tunnel cavern is assessed to ensure it met safety and

design standards.

4.3.1. Monitoring data analysis of clearance convergence

The change curves of the clearance convergence displacement and rate of monitoring points at the K27+180 section is shown in Figs. 16 and 17. Several key patterns can be observed from the clearance convergence monitoring at this section.

The first pattern observed was the significant deformation of the surrounding rock after excavation. The monitoring results indicate that the vault settlement changes particularly during the early stage from 1 day to 20 days after the instruments are installation. During this time,

H. Zhang et al. Results in Engineering 26 (2025) 104718

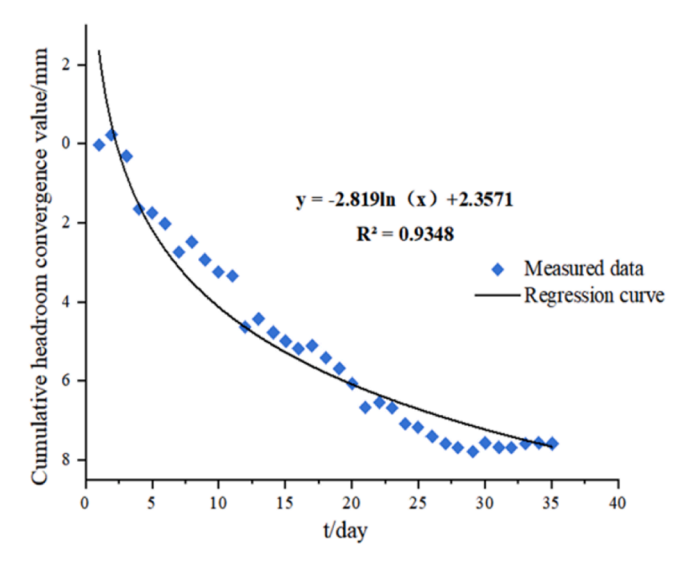


Fig. 16. Clearance convergence displacement curve.

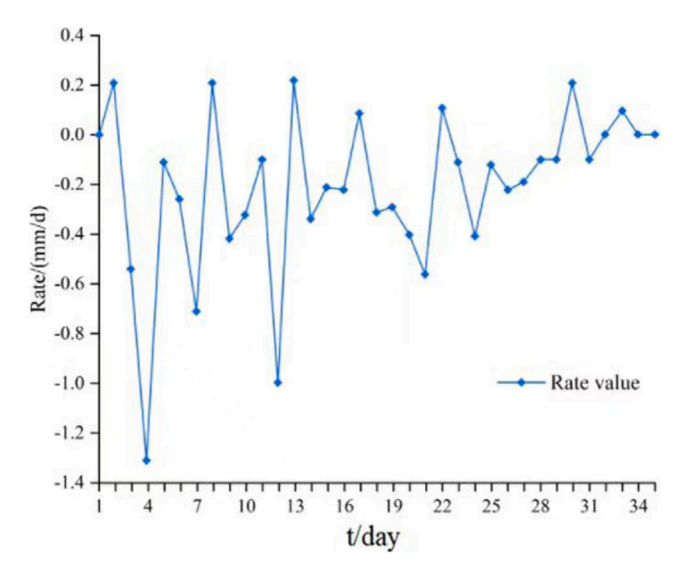


Fig. 17. Clearance convergence rate curve.

the settlement is about 0.2–0.4 mm per day. As the tunnel face moves further away from the monitored section, the influence on the section where the monitoring points are arranged is gradually weakened. From 25 day to 35 day, the horizontal displacement stabilizes at around 0.1 mm, with minimal change, indicating stable clearance convergence.

In addition, rapid initial deformation and high deformation rate are observed. The deformation rate is high in the early and middle stages after excavation, but it tends to be stable in the later stage. The maximum clearance convergence rate reaches 1.31 mm per day. The high deformation rate reveals the fast pressurization and relatively high pressure of the surrounding rock in the tunnel carbon, as well as its poor stability and self-stabilization ability.

Furthermore, the deformation takes a long time to be stable. The surrounding rock continues to deform over an extended period before reaching stability. Even after the completion of supporting works, the deformation of the surrounding rock does not cease immediately, and the deformation rate decreases gradually.

This analysis implies that after tunnel excavation, the surrounding rock undergoes large and fast deformation, with high initial deformation rate, and a prolonger stabilization period. The changes become pronounced as excavation approaches the fault fracture zone, highlighting

the need for enhanced monitoring and measurement efforts in these areas to ensure the safety of the tunnel construction.

4.3.2. Comparative analysis of simulation results

The field monitoring and measurement data of the K27+180 section of the subway tunnel, which crosses the fault fracture zone, are compared with the numerical simulation results obtained both with and without grouting reinforcement. Without grouting reinforcement, the numerical simulation predicted a final vault settlement and horizontal convergence value are 25 and 27 mm, respectively. After grouting reinforcement, the simulation results showed a significant reduction in these values, with the final vault settlement decreasing to 12 mm and horizontal convergence value to 13 mm. When these simulated results are compared with the actual field monitoring data, there is a strong correlation between the post-grouting reinforcement simulation and the field observations. Both the field data and the numerical simulation indicate a similar pattern: the displacement of the surrounding rock around the tunnel increases progressively as excavation advances. This correlation is visually depicted in Figs. 18 and 19.

Despite some differences between the field monitoring data and the numerical simulation results, both methods reveal a consistent pattern of gradual increase in the displacement of the surrounding rock around the tunnel with tunnel excavation. The differences between field monitoring data and numerically simulated data might be attributed to the restriction caused by the construction conditions as the initial support and field monitoring points are not installed timely.

5. Conclusion

In this research integrated field monitoring and advanced numerical simulation techniques to thoroughly investigate the engineering stress and deformation patterns of surrounding rock within the fault fracture zone of the Qingdao subway tunnel project. The effectiveness of advanced pre-grouting measures in controlling these factors are also assessed. Ultimately, this study yielded the following key conclusions:

• Without grouting reinforcement, the porewater pressure and seepage velocity changed significantly due to the instability of the surrounding rock in the fault zone during tunnel excavation. The maximum principal stress value of the initial support was 11 MPa, which was considerably greater than the design tensile strength of concrete, indicating severe potential safety hazards during construction. After grouting reinforcement measures were taken, the changes in the porewater pressure and seepage velocity decreased significantly. The maximum principal stress value of the initial support reduced to 4.7 MPa, a decrease of 57.27 % compared to the

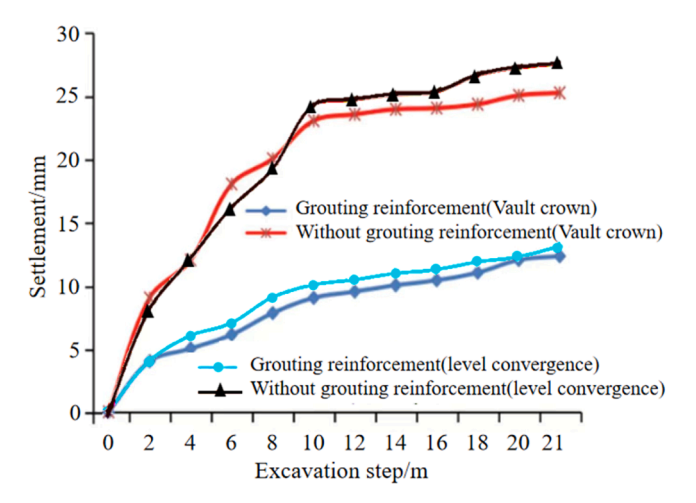


Fig. 18. Simulated value of vault settlement, and horizontal convergence.

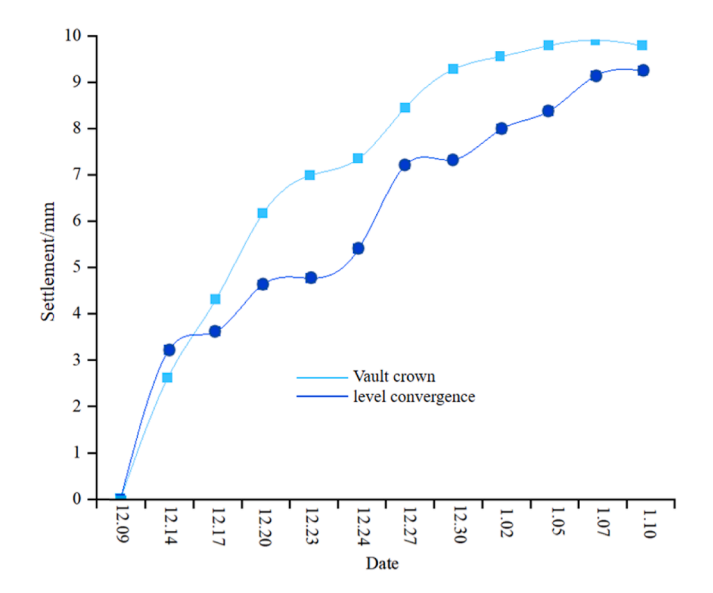


Fig. 19. Field monitoring data of vault settlement, and horizontal convergence.

scenario without grouting reinforcement. This finding clearly demonstrates that grouting reinforcement markedly enhances the safety and stability of tunnel construction in faults fracture zones.

- Comparison of the results with and without grouting reinforcement indicated that the maximum principal stress of the surrounding rock in the tunnel consistently appeared at the vault and tunnel bottom, leading to the subsidence of the tunnel vault and the uplift of the tunnel bottom. The minimum principal stress was observed at the left and right arch waists, resulting in inward extrusion of side walls and displacement. The findings provide a theoretical basis for key point monitoring and support strengthening during tunnel construction.
- The field-monitored maximum clearance convergence value and the vault settlement value were 7.81 mm and 7.2 mm, respectively, aligning with the three numerical results after progressive grouting treatment under the seepage field-stress field-displacement field coupling action. This cross-validation indicates that the grouting reinforcement measures have a good control effect, ensuring tunnel construction safety. The numerical modeling and careful parameter selection demonstrated high accuracy, providing a robust theoretical foundation for future engineering practice in similar environment.

This study is valuable for ensuring the construction safety of the subsea tunnel crossing the fault fracture zone. However, given the complexity of this engineering problem and the limitations in the numerical calculation boundary and parameters, this simulation only considered the influence of grouting reinforcement on the stability of the surrounding rock in the tunnel, without accounting for other construction. Future research should explore the stability of surrounding rock under varying construction conditions to gain a more comprehensive understanding of how tunnel rock stability is influenced by multiple factors, beyond just grouting reinforcement.

Funding

This work is financially supported by the National Natural Science Foundation of China (42172322), the Key Research and Development Project of the Department of Science and Technology in Henan Province of China (grant no 232102241040), and the Huanghuai University Cultivation Fund Project (grant no XKPY-2022017).

CRediT authorship contribution statement

Hui Zhang: Writing - original draft, Visualization, Validation,

Project administration, Methodology, Investigation, Formal analysis, Conceptualization. Majed A.A. Aldahdooh: Writing – review & editing, Conceptualization. Yong Hui Shang: Writing – review & editing, Funding acquisition. Hang Yin: Writing – original draft, Resources, Funding acquisition. Mohammed J.K. Bashir: Writing – review & editing. Ai Wei Wong: Writing – review & editing. Abdullateef Ashola Olanrewaju: Writing – review & editing, Supervision. Choon Aun Ng: Writing – review & editing, Supervision.

Declaration of competing interest

The authors declare that they have no known competing financial interests or personal relationships that could have appeared to influence the work reported in this paper.

Data availability

Data will be made available on request.

References

- X. Chen, Current situation and reflections on low-carbon and sustainable development of tunnels and underground engineering, Modern Tunnell. Technol. 61 (2024) 5–17. http://www.xdsdjs.com/CN/Y2024/V61/12/5 (accessed August 26, 2024).
- [2] Q. Pan, D. Dias, Three dimensional face stability of a tunnel in weak rock masses subjected to seepage forces, Tunnell. Undergr. Space Technol. 71 (2018) 555–566, https://doi.org/10.1016/i.tust.2017.11.003.
- [3] H. Zhang, X. Niu, G. Liu, Liu. Qiuyang, L. Miao, Liu Weixiong, Research on the dynamic response of the closely-attached underpass induced by the trains' vibrating load of metro, Chin. J. Rock Mech. Eng. 42 (2023) 1273–1286. http://ro ckmech.whrsm.ac.cn/CN/Y2023/V42/I5/1273 (accessed August 26, 2024).
- [4] Y. Shang, L. Shang, Q. Fang, Y. Zhao, Mean and non-Mean models for the safety evaluation of surrounding rock based on shield driving under a flyover structure, Modern Tunnell. Technol. 52 (2017) 121–128. http://www.xdsdjs.com/CN/art icle/downloadArticleFile.do?attachType=PDF&id=9595 (accessed August 26, 2024).
- [5] J. Yang, C. Wang, Y. Huang, C. Qin, W. Chen, Variation law of segment strain increment of an underwater shield tunnel during normal operation, Rock Soil Mech. 43 (2022) 2253–2262. http://ytlx.whrsm.ac.cn/EN/10.16285/j.rsm.2021 1752 (accessed August 26, 2024).
- [6] Y. Liu, Research on the key technology of Changsha Metro Cross-river Tunnel through Karst Stratum, J. Railway Eng. Soc. 37 (2020) 76–80.
- [7] Z. Li, C. He, Z. Chen, S. Yang, J. Ding, Y. Pen, Study of seepage field distribution and its influence on urban tunnels in water-rich regions, Bull. Eng. Geol. Environ. 78 (2019) 4035–4045, https://doi.org/10.1007/s10064-018-1417-0.
- [8] Z. Ye, Q. Jiang, C. Zhou, Y. Liu, Numerical analysis of unsaturated seepage flow in two-dimensional fracture networks, Int. J. Geomech. 17 (2017), https://doi.org/ 10.1061/(ASCF)CM.1943-5622.0000826
- [9] X. Liu, P. Lin, G. Han, G. He, Hydro-mechanical coupling process on rock slope stability based on discontinuous deformation analysis and discrete fracture network models, Chin. J. Rock Mech. Eng. 32 (2013) 1248–1256. http://rockmech. whrsm.ac.cn/EN/volumn/volumn_1401.shtml#1 (accessed August 26, 2024).
- [10] Y. Geng, P. Fang, Z. Jing, B. Liang, G. Tang, Study on surface subsidence characteristics of super large diameter pipe jacking construction in soft ground based on modified Peck formula, J. Hunan City Univ.: Nat. Sci. 32 (2023) 7–14. https://qikan.cqvip.com/Qikan/Article/Detail?id=7110818551&from=Qi kan_Article_Detail (accessed August 26, 2024).
- [11] H. Pan, W. Su, G. Zhai, Cao Hong, G. Luo, Soil disturbance induced by shield advancing through a small radius path, Chin. J. Rock Mech. Eng. 36 (2017) 1024–1031. http://rockmech.whrsm.ac.cn/CN/abstract/abstract29836.shtml (accessed August 26, 2024).
- [12] H.-L. Fu, H.-S. Deng, Y.-B. Zhao, X.-B. Chang, H.-D. Yi, Study on the disturbance of existing subway tunnels by foundation sloping excavation, Appl. Sci. 13 (2023) 948, https://doi.org/10.3390/app13020948.
- [13] S. Bernat, B. Cambou, P. Dubois, Assessing a soft soil tunnelling numerical model using field data, Géotechnique 49 (1999) 427–452, https://doi.org/10.1680/ geot.1999.49.4.427.
- [14] W. Mu, L. Li, D. Chen, S. Wang, F. Xiao, Long-term deformation and control structure of rheological tunnels based on numerical simulation and on-site monitoring, Eng. Fail. Anal. 118 (2020) 104928, https://doi.org/10.1016/j. engfailanal 2020 104928
- [15] Q. Di, P. Li, M. Zhang, C. Guo, F. Wang, J. Wu, Three-dimensional theoretical analysis of seepage field in front of shield tunnel face, Undergr. Space 7 (2022) 528–542, https://doi.org/10.1016/j.undsp.2021.11.006.
- [16] Z. Wei, Y. Zhu, A theoretical calculation method of ground settlement based on a groundwater seepage and drainage model in tunnel engineering, Sustainability. 13 (2021) 2733, https://doi.org/10.3390/su13052733.

- [17] Z. Qin, Y. Wang, Y. Song, Q. Dong, The analysis on seepage field of grouted and shotcrete lined underwater tunnel, Math. Probl. Eng. 2020 (2020) 1–15, https:// doi.org/10.1155/2020/7319054.
- [18] Y. Hu, H. Lei, G. Zheng, L. Shi, T. Zhang, Z. Shen, R. Jia, Assessing the deformation response of double-track overlapped tunnels using numerical simulation and field monitoring, J. Rock Mech. Geotechn. Eng. 14 (2022) 436–447, https://doi.org/ 10.1016/j.jimpa.2021.07.003
- [19] X. Song, F.-Y. Meng, R.-P. Chen, H.-L. Wang, H.-N. Wu, Effect of seepage on soil arching effect in deep shield tunnel, Undergr. Space 12 (2023) 218–233, https://doi.org/10.1016/j.undsp.2023.02.011.
- [20] Z. Li, Z. Chen, C. He, C. Ma, C. Duan, Seepage field distribution and water inflow laws of tunnels in water-rich regions, J. Mt. Sci. 19 (2022) 591–605, https://doi. org/10.1007/s11629-020-6634-x.
- [21] Y. Zhang, D. Zhang, Q. Fang, L. Xiong, L. Yu, M. Zhou, Analytical solutions of non-Darcy seepage of grouted subsea tunnels, Tunnell. Undergr. Space Technol. 96 (2020) 103182, https://doi.org/10.1016/j.tust.2019.103182.

- [22] Ishimaru, Maintenance management of Kanmon Tunnel in Japan (C. Zhou, Trans.), Collect. Tunnel Transl. 5 (1981) 6–12.
- [23] M. Qian, X. Miao, L. Li, Mechanism for the fracture behaviours of main floor in Longwall mining, Chin. J. Geotechn. Eng. 17 (1995) 55–62. http://cge.nhri.cn/en/article/id/9914 (accessed August 26, 2024).
- [24] D. Wang, Q. Zhang, X. Zhang, Z. Li, P. Zhao, D. Zheng, Research and application on tunnel and underground engineering grouting effect of the fuzzy evaluation method, Chin. J. Rock Mech. Eng. 36 (2017) 3431–3439.
- [25] J. Tinoco, A.G. Correia, P. Cortez, Application of data mining techniques in the estimation of the uniaxial compressive strength of jet grouting columns over time [J], Construct. Build. Mater. 25 (3) (2011) 1257–1262.
- [26] S. Srijan, A K.A Gupta, Basic study on ground improvement techniques and its applications[C], in: International Conference on the Asian Civil Engineering Coordinating Council, Singapore, Springer, 2024.